JOURNAL OF MATERIALS SCIENCE 33 (1998) 1591–1606

Comparison of the fatigue propagation behaviour of polystyrene and 95/5 polystyrene/polyethylene blends

M. N. BUREAU*, J. I. DICKSON
Département de Métallurgie et de Génie des Matériaux, École Polytechnique C.P. 6079, Succ. Centre-Ville, Montréal, Canada, H3C 3A7
E-mail: martin.bureau@nrc.ca.

J. DENAULT
Institut des Matériaux Industriels, Conseil National de Recherche Canada, 75 de Mortagne, Boucherville, Canada, J4B 6Y4

The fatigue crack propagation (FCP) behaviour of polystyrene (PS) and 95/5 PS/high density polyethylene (HDPE) was studied at cycling frequencies (f) of 0.2, 2 and 20 Hz. At the latter two frequencies, the fatigue crack growth rates (FCGRs) in the blends were lower than in PS, especially when a styrene/ethylene–butylene/styrene (SEBS) triblock copolymer was added as a compatibilizer. The fractographic features observed were analysed in detail. Discontinuous growth bands (DGBs), associated with the fracture of crazes, formed at low FCGRs in PS and at low and high FCGRs in the blends. Large dimple-like features formed at intermediate FCGRs and fatigue striations at high FCGRs were observed in PS. The observations indicated that the reduction in FCGR when HDPE was added to PS was associated with the presence of stretched HDPE particles which fractured behind the crack front, with increased particle–matrix adhesion favoured by the compatibilizer. An increase in cycling frequency decreased the FCGRs, with the fractographic observations indicating that this effect was associated with a decrease in the time-dependent deformation in the fracture process zone slightly ahead of the crack tip.

1. Introduction

Blends, in which rubber is added to a glassy thermoplastic such as polystyrene, are well known for their improved mechanical properties, particularly their impact strength [1]. More recently, blends of low glass transition temperature thermoplastics, such as polyethylene (PE) or polypropylene (PP), as the minor phase in glassy thermoplastics have been developed [2–10]; however, a well-dispersed distribution of minor phase particles with a diameter of approximately 1–5 μm as well as a high strength particle–matrix interface are required in order to obtain significant toughening effects in multiple crazing conditions [11–17]. Because of the importance of fatigue failures in practical applications, a good understanding of the fatigue crack propagation behaviour of polymer blends is desirable.

A number of studies [18–33] have considered the behaviour of thermoplastic polymers under cyclic loading. Discontinuous growth bands (DGBs) have been observed on the fracture surfaces at low cyclic stress intensity factors, ΔK [18], and have been associated with crazed material in the cyclic plastic zone r_p [18–20]. Some authors reported a second degree power-law relationship between the DGB spacing and ΔK [18, 34–36], in agreement with the Dugdale plastic zone size [37] given by

$$r_p = \frac{\pi}{8}\left(\frac{K_{max}}{\sigma_y}\right)^2 \quad (1)$$

where K_{max} is the maximum stress intensity factor and σ_y is the conventional tensile strength, while others [35, 38, 39] have reported a linear relationship between the DGB spacing and ΔK. In such DGBs, crack tip opening displacement (COD) measurements have indicated that only a fraction (1/2 to 2/3) of the craze is fractured during a discontinuous crack propagation event and that a new craze is formed simultaneously with crack propagation through the former craze [39, 40].

Fatigue striations, characterized by an interstriation spacing in agreement with the macroscopic fatigue crack growth rate (FCGR) [25, 36], suggesting that a striation is formed during each stress cycle, have also been reported on the fracture surface of various polymers at relatively high ΔK [29, 36, 41]. Over

* Author to whom correspondence should be addressed.

a wider range of ΔK, however, some results have indicated that the striation spacing does not always agree with the macroscopic FCGR [31, 42, 43].

In pre-notched specimens, a decreasing FCGR with increasing cycling frequency f has been observed, usually for thermoplastic polymers showing a secondary viscoelastic transition (β-peak) at the fatigue testing temperature and frequency [18, 20, 21, 34, 44–50]. An increase in fatigue crack propagation (FCP) resistance with increasing f is designated as a positive frequency effect. When a secondary viscoelastic transition is not observed in the fatigue testing conditions, however, the FCGR does not usually vary with f [21, 25, 51]. Since the β-peak represents a region of maximum loss compliance, hysteretic heating caused by energy dissipation during fatigue loading should occur near this peak. In the case of confined deformation, as in plane strain FCP tests, a localized temperature rise in the plastic zone near the crack tip may occur. With a significant increase in temperature, yielding in the material near the crack tip should be enhanced, leading to an increase in crack tip radius. It has been argued that the FCGR can be expected to be lowered [26], as a result of the crack tip region experiencing a lower effective ΔK. However, despite the general agreement between the presence of a β-peak secondary viscoelastic transition and the frequency effect on FCGR, very few experimental observations of a significant temperature rise in the crack tip region accompanying FCGR reduction with increasing f have been reported [30, 52].

The objectives of this paper are to investigate the FCP behaviour of polystyrene (PS) and of blends of PS with 5% high density polyethylene (HDPE), to identify the mechanisms of fatigue propagation by means of fractographic observations and to verify and explain the existence of a loading frequency effect on the FCGR. The effects of a styrene/ethylene-butylene/styrene (SEBS) triblock copolymer added as a compatibilizer in order to increase the PS/HDPE interface cohesion [3–7, 53–58] are also discussed.

2. Experimental procedure

2.1. Material preparation

The materials employed were a high density polyethylene HBL-455A ($\bar{M}_w$ = 171 000, $\bar{M}_w/\bar{M}_n$ = 20.3, where $\bar{M}_w$ and $\bar{M}_n$ are respectively the weight average and the number average molecular weight), an atactic extrusion grade polystyrene GPPS103 ($\bar{M}_w$ = 270 000, $\bar{M}_w/\bar{M}_n$ = 2.0) supplied by Novacor, and a styrene/ethylene–butylene/styrene triblock copolymer Kraton™ G1652 as compatibilizer supplied by Shell Development Co. These polymer grades were chosen for their melt viscosity ratio approaching unity at high shear rates [10]. They were blended at 200 °C in a 34 mm Leistritz co-rotating twin screw extruder, with the screw speed set at 180 r.p.m. The screw configuration consisted of a melting zone composed of eight kneading discs staggered at + 60° followed by four discs staggered at − 30° and a mixing zone composed of two pairs of 7.5 mm discs staggered at 90°. No reverse element was employed. Two groups of granulated blends were obtained, the first containing no compatibilizer, and the second containing 10% of SEBS compatibilizer by weight of the minor phase (i.e. HDPE), added to this phase before the PS/(SEBS/HDPE) blending in order to optimize the compatibilization. The composition of the blend without the addition of SEBS was 95/5 PS/HDPE and the composition of the blend with SEBS was 95/(4.5/0.5) PS/(HDPE/SEBS). The blends were injection-molded into 75 × 100 mm plates with a thickness of 5 mm. An Engel 75-tonne injection machine was employed at a constant flow rate of 63.5 mm s^{-1}. A relatively high melt temperature at the injection nozzle of 265 °C was used due to the extrusion grade nature of the PS employed. The temperature of the mould was 65 °C. The holding pressure was set at 2 MPa and the holding time was 10 s.

2.2. Dynamic testing

Dynamic shear modulus measurements were performed on PS specimens using a Rheometrics model 605 rheometric mechanical spectrometer. The tests were done at frequencies of 1 and 16 Hz over a temperature range extending between − 40 °C to + 100 °C, with the test temperature increasing at a constant rate of 2 °C min^{-1}. The applied strain was 0.2% in rotation. For these RMS measurements, the pellets were vacuum-dried for 12 h at 75 °C, before the specimens were compression-moulded at 210 °C into 3 × 12 × 45 mm bars.

2.3. Tensile testing

Tensile stress–strain tests were performed following ASTM D-638 standard test method at 23 °C using a computer-controlled Instron tester. The crosshead speeds employed were 0.5, 5 and 50 mm min^{-1} which resulted in engineering strain rates of 3×10^{-4}, 3×10^{-3} and 3×10^{-2} s^{-1}, respectively. A longitudinal extensometer 25.4 mm in length was employed to measure the engineering strain. The reduced section of the tensile specimens conformed to ASTM D-638 type IV specimens, with the overall length being 75 mm. The specimen thickness was that of the moulded plates (5 mm). Young's modulus was estimated at very low strain (< 0.4%) by the tangent modulus of elasticity. Young's modulus, the tensile strength and the tensile strain (i.e. the engineering stress and strain reached when the load is maximum) and the engineering strain at failure reported are averages determined from four to eight tests. Standard deviation of the reported values was lower than 5%.

2.4. Fatigue crack propagation testing

The FCP tests were performed at 23 °C and 50% of humidity following the ASTM E-647 standard test method, employing a computer-controlled servo-hydraulic Instron tester, a sinusoidal waveform, a cycling frequency of 2 and 20 Hz and a R-ratio ($R = P_{min}/P_{max}$, where P_{min} and P_{max} are, respectively, the minimum and maximum load applied) of 0.1. Compact

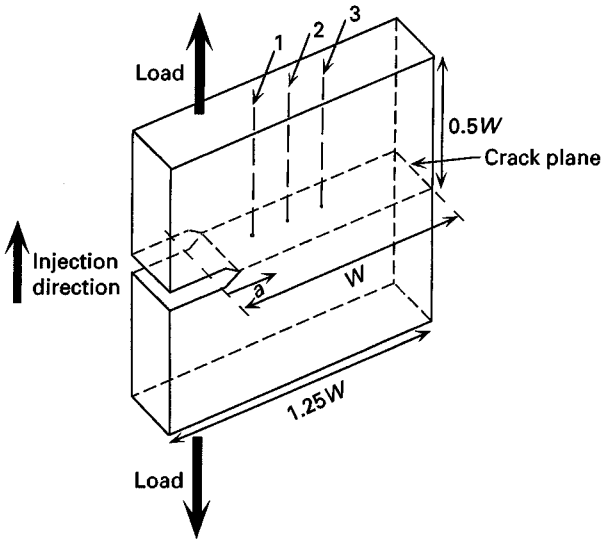

Figure 1 Schematic representation of the CT specimens employed for the FCP tests with the injection direction parallel to the loading axis. The locations of thermocouples at times employed are indicated by thin arrows 1, 2 and 3.

tension (CT) specimens (Fig. 1) were employed, with a thickness B equal to that of the injection-moulded plates (5 mm), a specimen width W of 50 mm, a notch depth of 9 mm and a notch opening width of 2.5 mm. A razor-blade cut was introduced manually at the notch tip just prior to the start of precracking. The specimens were loaded for propagation normal to the injection direction (Fig. 1). On-line crack length monitoring was performed employing the compliance method, with the compliance measured by a clip-on COD gauge. Each fatigue crack growth rate measurement was obtained over a minimum propagation distance of 0.15 mm. The crack length a was also measured manually using a traveling microscope to verify the crack length monitoring by the compliance method. The measured compliance function U was converted into crack length using the appropriate equation taken from ASTM E-647. All specimens were precracked at $R = 0.1$ under constant ΔK such that the final K_{max} in precracking was less than the minimum K_{max} value of the following FCP test. A ΔK gradient of 0.09 mm^{-1} given by $(K^{-1})(dK/da)$ was employed to generate ΔK data.

A second set of FCP tests at three frequencies (0.2, 2 and 20 Hz) and at three constant ΔK values of 0.3, 0.65 and 0.9 $MPa\,m^{1/2}$ was performed on each specimen, starting at the lowest ΔK value and finishing at the highest value. The crack propagation data were obtained over a minimum distance of 2 mm for each test condition. Similar tests were also performed on modified CT specimens, in which side grooves 0.45 mm in depth were present along the crack plane, in order to eliminate any effect of the oriented skin in these specimens obtained from injection moulding.

2.5. Crack tip temperature rise measurements

The rise in temperature at the crack tip was monitored by two methods. The first consisted of crack tip temperature measurements using an Agema 900 infrared camera with a spectral range of 8 to 12 μm, a thermal sensitivity of 0.08 °C at 30 °C and an accuracy of 1 °C. The spatial resolution was 660 μm horizontally and 550 μm vertically. The second method consisted of crack tip temperature measurements using 1 mm-diameter copper–Constantan thermocouple probes with an accuracy of 0.2 °C inserted into the CT specimens and positioned at the mid-thickness at three different sites on the expected crack plane, as shown in Fig. 1.

2.6. Fractographic observations

The fatigue fracture surfaces were first coated with gold–palladium and then observed with a JEOL JSM-6100 scanning electron microscope (SEM). The size and shape of the fractographic features reported were evaluated, in most cases, on stereographic observations obtained using two photographs with a 6° difference of tilt angle. Observations on matching fracture surfaces were also carried out to determine the fracture surface profile. Computer-assisted image analysis was employed to evaluate the surface density of HDPE particles (number of HDPE particles per unit area) on the FCP fracture surface of the compatibilized and non-compatibilized PS/HDPE specimens. The lowest particle count employed was 400.

3. Results and discussion

3.1. Viscoelastic spectrum

The RMS technique was employed to verify for the presence of a secondary viscoelastic transition in the testing conditions. The viscoelastic spectrum of the PS matrix is shown in Fig. 2 for two different testing frequencies. Around the testing temperature (e.g. 23 °C), a change in the damping ratio ($\tan\delta = E''/E'$, with E'' being the loss modulus and E' the storage modulus) to a maximum value of 1.5×10^{-2} and 1.1×10^{-2} was observed at 1 and 16 Hz, respectively.

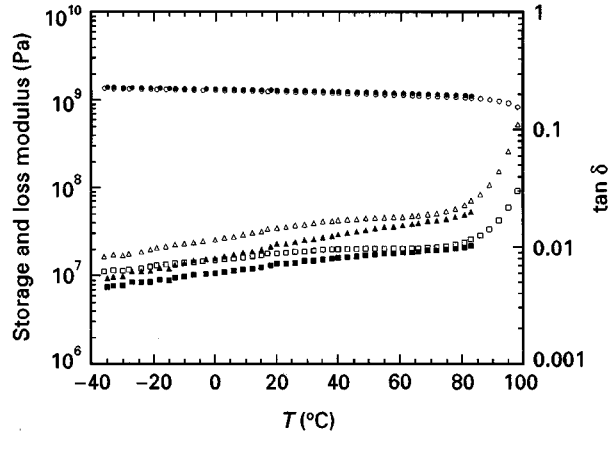

Figure 2 Viscoelastic spectra for pure PS showing the variation of the storage shear modulus G' (○, ●), the loss shear modulus G'' (□, ■) and the damping ratio $\tan\delta$ (△, ▲) with the testing temperature T at a testing frequency of 1 Hz (open symbols) and 16 Hz (closed symbols).

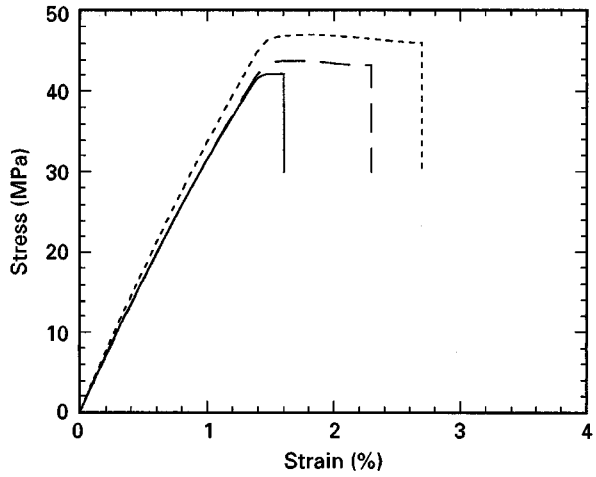

Figure 3 Engineering tensile stress–strain curves for pure PS specimens at engineering strain rates of 3×10^{-4} (——), 3×10^{-3} (— — —) and $3 \times 10^{-2}\,s^{-1}$ (– – –).

However, the hysteretic heating being proportional to the tan δ value at the testing temperature and frequency [59, 60] and limited to the cyclic plastic zone, a relatively low temperature rise in the crack tip region during FCP tests is expected. This indicates the presence of a weak β-peak transition near room temperature in PS for both frequencies, as already reported by Illers [61].

3.2. Tensile behaviour

A representative engineering stress-strain curve for the three strain rates employed is shown in Fig. 3 for the PS specimens. As expected, higher strain rates lead to higher Young's modulus, tensile strength, tensile strain and strain at failure. However, the tensile test results reported in Table I indicate that the strain rate has only a limited effect on the tensile behaviour. Increasing the strain rate by two orders of magnitude results in an increase of less than 5% in Young's modulus and less than 13% in the tensile strength. In general, amorphous polymers are known to be little affected by the strain rate because of the limited reorientation during deformation as a result of their high rigidity and entanglement density [62].

Table I also shows that the addition of HDPE to the PS matrix reduces Young's modulus and the tensile strength, similar to results in rubber-toughened blends such as high impact polystyrene (HIPS) [63]. However, the addition of HDPE does not lead to an increased fracture strain, in contrast to the very large strain at fracture obtained for HIPS specimens. The low ductile phase content in the 95/5 PS/HDPE specimens tested, compared to that of HIPS (typically 20 to 30%), may explain this lack of toughening effect. A previous study [10] has shown that a considerable increase in toughness and fracture strain is obtained for higher HDPE contents.

3.3. FCP behaviour

FCP tests at increasing ΔK with a constant ΔK gradient were performed at 2 and 20 Hz. The FCGR (da/dN, where N is the number of cycles) plotted against ΔK on a log–log scale are shown in Fig. 4 for PS and compatibilized and non-compatibilized PS/HDPE specimens. This figure shows the constant power-law regime or Paris regime [64] described by the following relationship

$$\frac{da}{dN} = A\Delta K^n \qquad (2)$$

where A and n are material constants. The results show that the crack growth rate increases with decreasing f, in agreement with previous results obtained for PS and rubber-toughened poly(phenylene oxide) (PPO)/PS blends [21, 34]. The FCP results also showed less experimental dispersion at 2 Hz than at 20 Hz.

Additional FCP tests were performed for each material at three constant ΔK values (0.3, 0.65 and 0.9 MPa $m^{1/2}$) for three cycling frequencies (0.2, 2 and 20 Hz). Power-law regressions were obtained to compare the FCP behaviour of each material based on at least 30 da/dN–ΔK experimental points at each f. The A and n values obtained from Equation 2 are presented in Table II, with the exponent n corresponding to an almost constant value of 2.6. Thus, this material constant does not seem to be affected by f, by

TABLE I Tensile test results at engineering strain rates of 3×10^{-4}, 3×10^{-3} and $3 \times 10^{-2}\,s^{-1}$ for PS and compatibilized and non-compatibilized 95/5 PS/HDPE

Material	Engineering strain rate (s^{-1})	Young's modulus (GPa)	Tensile strength (MPa)	Tensile strain (%)	Strain at failure (%)
PS	3×10^{-4}	3.4	42	1.4	1.6
	3×10^{-3}	3.4	44	1.4	2.4
	3×10^{-2}	3.5	47	1.5	2.7
Non-compatibilized 95/5 PS/HDPE	3×10^{-4}	3.0	40	1.6	1.6
	3×10^{-3}	3.0	41	1.7	1.8
	3×10^{-2}	3.1	44	1.7	1.8
Compatibilized 95/5 PS/HDPE	3×10^{-4}	2.9	40	1.7	1.7
	3×10^{-3}	3.0	42	1.7	1.9
	3×10^{-2}	3.0	45	1.7	2.2

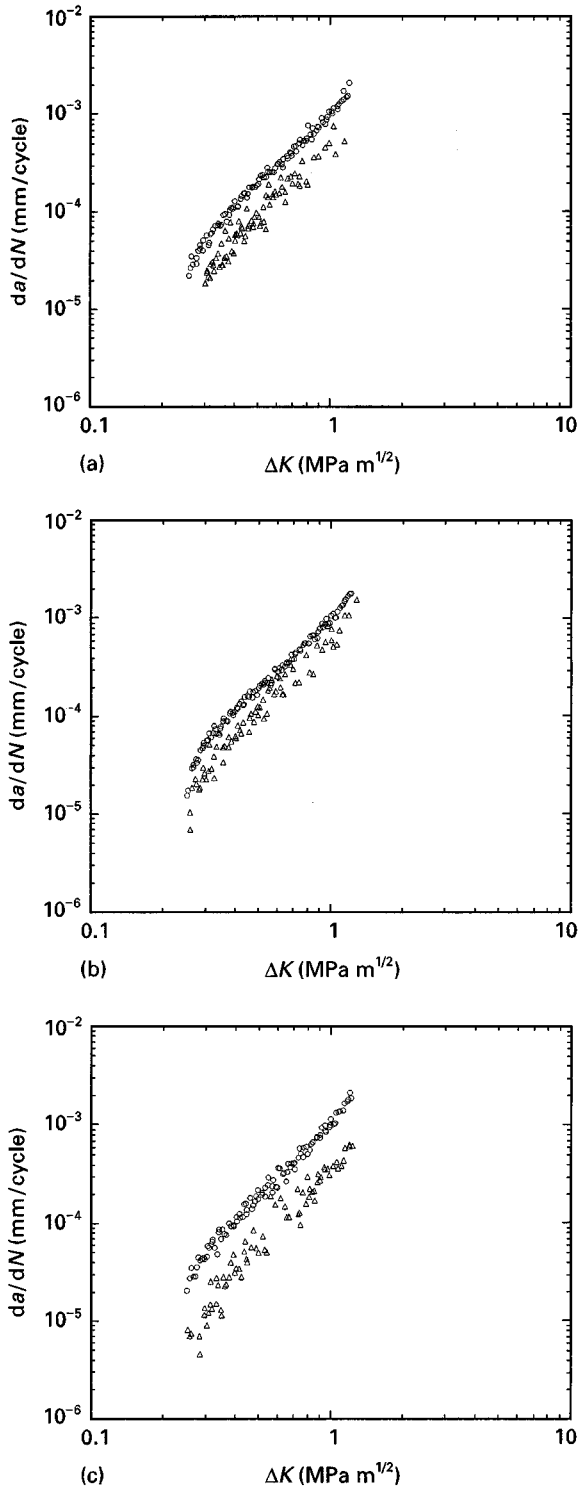

Figure 4 FCP curves showing $\log da/dN$ plotted against $\log \Delta K$ at 2 (○) and 20 Hz (△) for: (a) pure PS; (b) non-compatibilized 95/5 PS/HDPE; and (c) compatibilized 95/5 PS/HDPE.

the presence of HDPE nor by the addition of SEBS. This value of n can be compared to values of 2.8 to 4.3 previously reported for PS [21, 25, 26, 65]. Table II also indicates that the constant A decreases with increasing f, with the FCGR reduced by approximately a factor of 2 to 2.5 when f is increased by a factor of 10. This factor is in agreement with that of 2.3 previously reported for PS [21, 34] and reflects the higher FCP resistance obtained with increasing f. Table II also suggests that the addition of HDPE, especially when compatibilized with SEBS, leads to

TABLE II Material constants, A and n, for the FCP relationship obtained for pure PS and compatibilized and non-compatibilized 95/5 PS/HDPE at cycling frequencies of 0.2, 2 and 20 Hz, including those of modified CT specimens (i.e. with side grooves present)

Material	f (Hz)	A	n
PS	0.2	2.6×10^{-3}	2.6
	2	1.3×10^{-3}	2.6
	20	6.6×10^{-4}	2.6
Modified CT specimen	20	7.6×10^{-4}	2.3
Non-compatibilized 95/5 PS/HDPE	0.2	2.6×10^{-3}	2.5
	2	1.1×10^{-3}	2.6
	20	5.1×10^{-4}	2.6
Modified CT specimen	20	5.7×10^{-4}	2.2
Compatibilized 95/5 PS/HDPE	0.2	2.2×10^{-3}	2.4
	2	1.0×10^{-3}	2.6
	20	3.5×10^{-4}	2.5
Modified CT specimen	20	4.5×10^{-4}	2.7

a small but significant increase in FCP resistance at 2 and 20 Hz, while at 0.2 Hz the effect is smaller. Also shown in Table II is that modification of the CT specimens by removing a 0.45 mm deep layer along the expected crack plane at the lateral surfaces also affected the FCP behaviour.

3.4. Crack tip temperature rise measurements

Neither the thermocouple probes inserted into the PS specimens in front of the crack tip nor the infrared camera employed to record the temperature rise on the surface of these specimens noted a temperature rise higher than 0.5 °C during the FCP tests. This temperature rise in the plastic zone in front of the crack tip should not be strong enough to significantly alter the mechanical behaviour of the polymer tested.

3.5. Fractographic observations

DGBs at low da/dN (typically up to $1\text{–}2 \times 10^{-4}$ mm/cycle), large dimple-like features at medium da/dN (typically from $1\text{–}2 \times 10^{-4}$ mm/cycle to $3\text{–}4 \times 10^{-4}$ mm/cycle) and striation-like features at high da/dN (typically greater than $3\text{–}4 \times 10^{-4}$ mm/cycle) were observed to be the dominant fractographic features associated with FCP in PS specimens as well as in compatibilized and non-compatibilized 95/5 PS/HDPE specimens. A schematic diagram of a typical FCP curve showing these three regions of fractographic features is presented in Fig. 5. Such a diagram showing only the DGB region on a FCP curve has been presented by Takemori [29].

3.5.1. PS specimens

The FCP fracture surface of the PS specimens showed the presence of DGBs at low FCGRs for all test frequencies, including in the precrack region. Observations of typical DGBs formed in the fatigue region

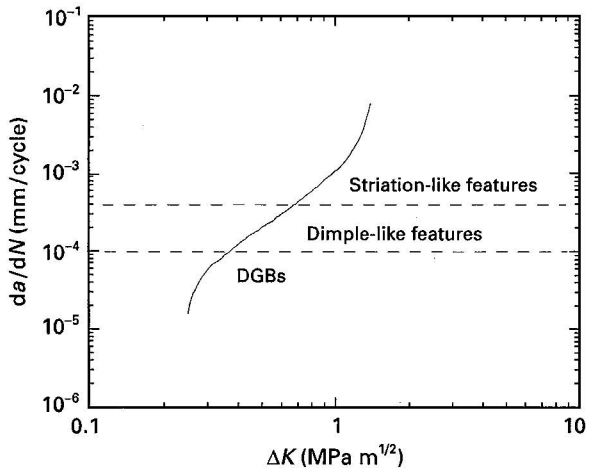

Figure 5 Schematic diagram of a typical FCP curve showing the region in which the formation of DGBs, of large dimple-like features and of striation-like features dominate. In the region of striation-like features, large dimple-like features are also present but decrease in quantity as da/dN increases.

of the PS specimens cycled at 2 and 20 Hz at a similar low ΔK (0.37 and 0.38 MPa m$^{1/2}$, respectively) and at relatively low FCGR (7×10^{-5} and 4×10^{-5} mm/cycle, respectively) are presented in Fig. 6. The DGB width is approximately 20 μm for both frequencies; however, the DGB fracture surface morphology is significantly influenced by f. The number of cycles associated with the DGB formation at this ΔK was evaluated as approximately 286 and 500 cycles at 2 and 20 Hz, respectively. The fracture surface of the DGBs produced at 2 Hz shows an important number of very thin elongated fibrils separating microvoids or dimples, while that produced at 20 Hz shows a considerably smaller number of fibrils and larger microvoids. These observations indicate that for a similar ΔK value more microvoids are nucleated in the crazed region ahead of the crack tip at the lower f, as previously reported by Hertzberg *et al.* [25], while at the higher f more growth of individual microvoids occurred prior to the crack advance. These observations suggest that at least at this ΔK level the nucleation of more microvoids at the lower f is responsible for the higher FCGR.

The width of the DGBs formed in PS specimens was measured for different ΔK (Fig. 7a). As previously mentioned, no effect of the test frequency on the width of the DGBs was noted. As shown by Fig. 7a, an important dispersion is noted in the width of the DGBs measured. This dispersion is not caused by the experimental measurements obtained from stereofractographs, but rather by the nature of the DGB formation. However, despite this large dispersion, it can be observed that the width of the DGBs varies with ΔK^i, with the i exponent being between 1 and 2.

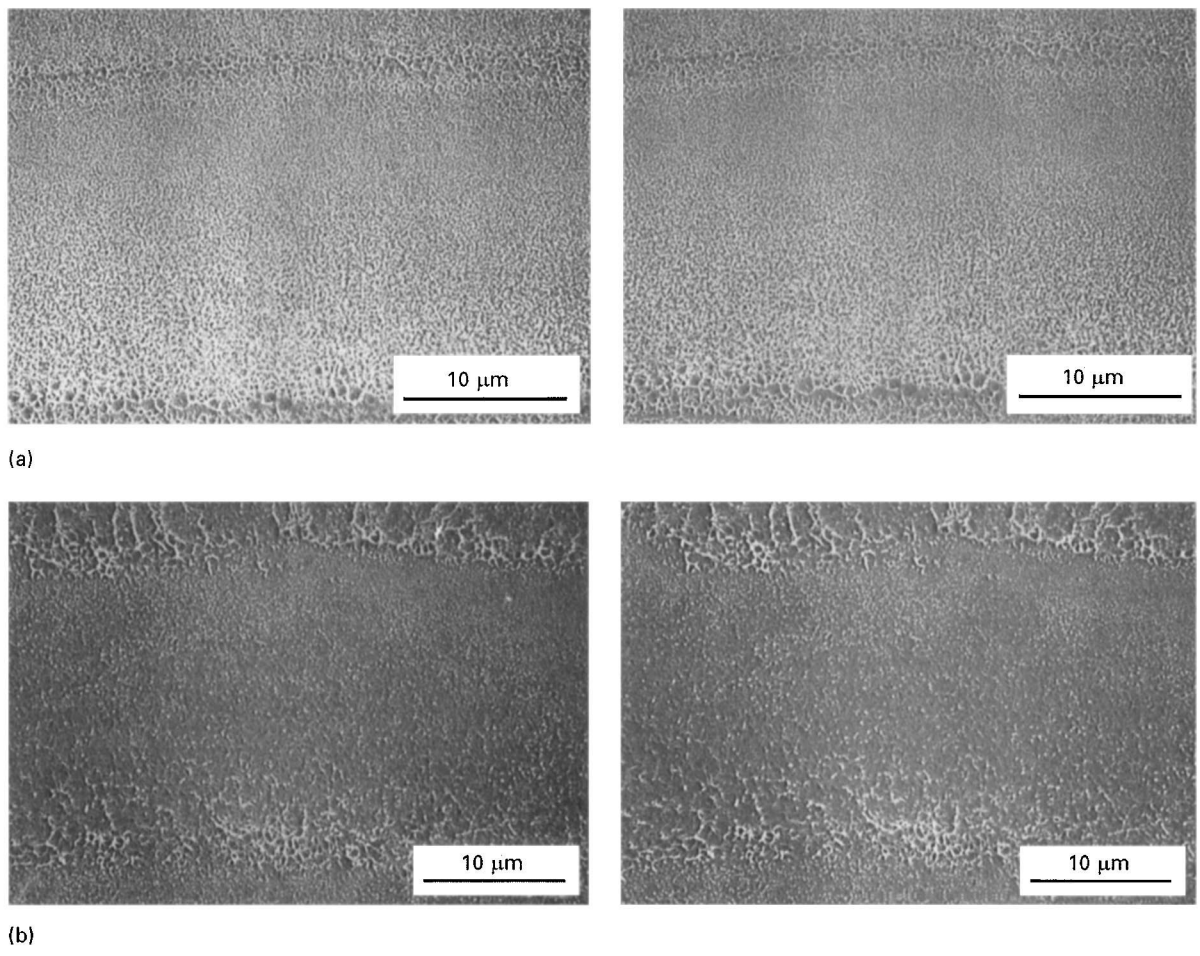

Figure 6 Stereofractographs of DGB's approximately 20 μm in width observed in PS specimens cycled at: (a) $\Delta K = 0.37$ MPa m$^{1/2}$, $da/dN = 7 \times 10^{-5}$ mm/cycle and $f = 2$ Hz; (b) $\Delta K = 0.38$ MPa m$^{1/2}$, $da/dN = 4 \times 10^{-5}$ mm/cycle and $f = 20$ Hz. The macroscopic FCP direction is from bottom to top.

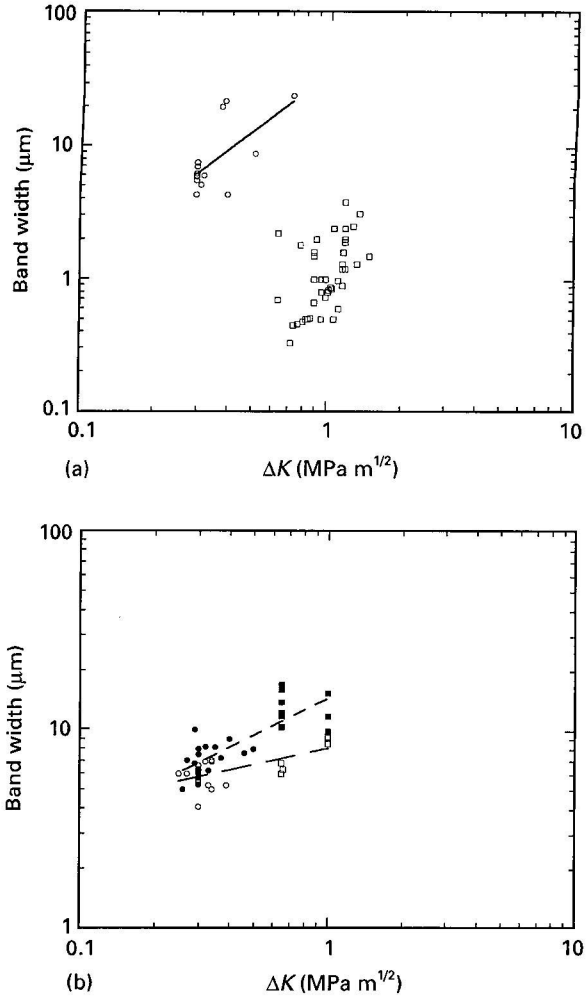

Figure 7 Band width (i.e. DGB width and interstriation spacing) plotted against ΔK on log–log scale at either 0.2, 2 or 20 Hz: (a) DGBs (○) and striation-like features (□) observed in PS specimens; (b) DGBs (○, ●) and striation-like features (□, ■) observed in 95/5 PS/HDPE specimens (open symbols represent non-compatibilized blends, closed symbols compatibilized blends). Power-law regressions are drawn for DGBs in PS (——) and for the DGBs and striation-like features in compatibilized (– – –) and non-compatibilized (— — —) 95/5 PS/HDPE specimens.

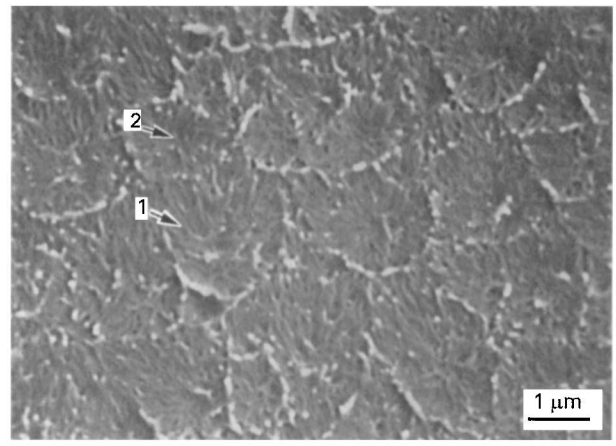

Figure 8 Large dimple-like features approximately 2 μm in diameter observed in a PS specimen for $\Delta K = 0.84\ \mathrm{MPa\,m^{1/2}}$, $da/dN = 8 \times 10^{-4}$ mm/cycle and $f = 2$ Hz presenting numerous fine U-shaped dimples (arrow 1) with the U-edge pointing towards a region of fine round dimples (arrow 2) near the centre of each large dimple-like feature. The macroscopic FCP direction is from bottom to top.

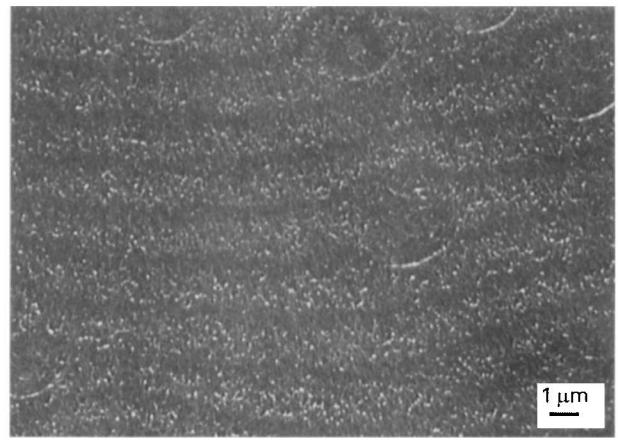

Figure 9 Striation-like features approximately 2 μm in width in a PS specimen for $\Delta K = 0.9\ \mathrm{MPa\,m^{1/2}}$, $da/dN = 2 \times 10^{-3}$ mm/cycle and $f = 0.2$ Hz showing the occasional presence of large dimple-like features. The macroscopic FCP direction is from bottom to top.

The average value of the exponent obtained was approximately 1.5, but there was considerable scatter in the results. This value can be compared with studies which found that the DGB spacing varies linearly with ΔK for polyvinyl chloride (PVC), polymethylmethacrylate (PMMA), polycarbonate (PC) and vinylurethane [38–40, 66], while other studies found that the DGB spacing varies with ΔK^2 in a variety of thermoplastic glassy polymers [18, 34–36]. Also shown in Fig. 7a are the striation-like spacing measurements as a function of ΔK, which are clearly not associated with the DGB formation.

For da/dN greater than $1–2 \times 10^{-4}$ mm/cycle, large dimple-like features (Fig. 8) covered the fracture surface, with these features presenting a number of finer dimples and elongated half-dimples. Stereographic observations of these large microvoids indicate the presence of elongated fibrils between them, which correspond to remnants of ligaments present in the region where the microvoids coalesced together. The average size of the large dimple-like features observed starting at approximately $da/dN = 2 \times 10^{-4}$ mm/cycle was found to increase with increasing da/dN from a size of approximately 1 μm for the lowest da/dN at which they formed to a size of approximately 3 μm for the da/dN at which striation-like features started to appear (Fig. 9). These large dimples contained a number of U-shaped smaller dimples (Fig. 8), typically 0.1–0.4 μm in width, although of longer length, with the centre of the U-edge pointing towards a region near the centre of the large dimple, but usually closer to the side from which the crack propagated. In this region, there were generally several small round dimples indicating that the large dimple had initiated locally. The small microvoids, which coalesced with the large microvoid as the latter grew, then had the part of their surface which initially faced away from this large microvoid transformed into the external surface of the microvoid after coalescence had occurred. This resulted in this portion of the microvoids not being visible as a dimple on the

fracture surface. Thus the small microvoids which coalesced with the larger growing microvoid produced U-shape dimples with the centre of the U-edge pointing towards the site at which this large dimple had started to form. These U-shaped dimples are therefore similar to U-shaped dimples which have coalesced with a stretch zone during the start of a ductile final fracture of a fatigue precracked metal.

For da/dN greater than $3–4 \times 10^{-4}$ mm/cycle, striation-like features (Fig. 9) also became present on the fracture surface, and the large dimples became progressively less numerous as da/dN increased. In the region in which dimples and striations were both present, a number of the large dimples were mostly aligned parallel to the striations (Fig. 10). In these regions (Fig. 11), the portion of the large dimples which grew in the direction opposite to the macroscopic crack growth direction had a well-marked boundary where they met the macroscopic crack front, while the remainder blended into the portion presenting striations with no boundary being observed.

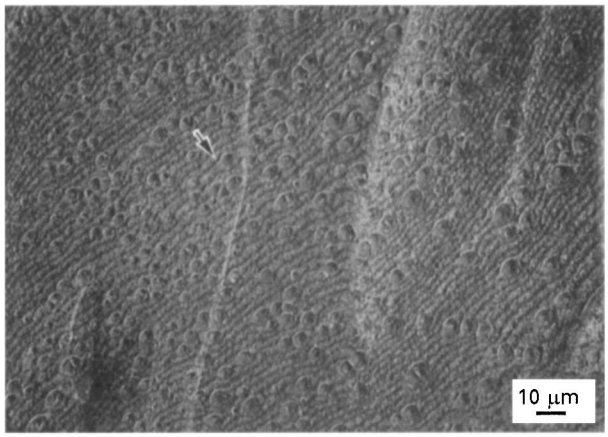

Figure 10 Striation-like features approximately 2 μm in width with large dimple-like features 1–3 μm in diameter aligned parallel to the striations in a PS specimen for $\Delta K = 0.9$ MPa m$^{1/2}$, $da/dN = 2 \times 10^{-3}$ mm/cycle and $f = 2$ Hz . The FCP direction is indicated by the arrow.

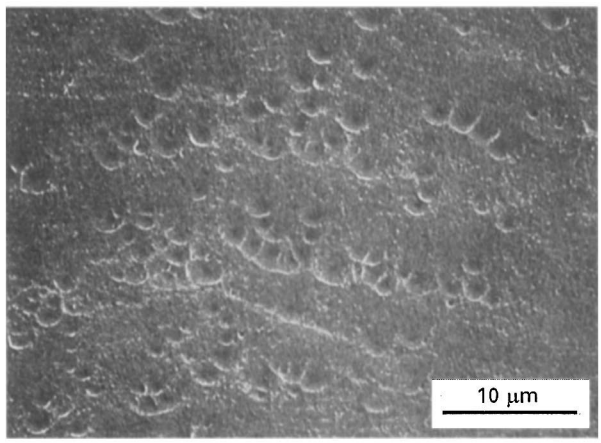

Figure 11 Ribbon-like groups of large dimples 1.5 μm in diameter aligned approximately parallel to striation-like features with an approximate width of 0.8 μm in a PS specimen for $\Delta K = 0.96$ MPa m$^{1/2}$, $da/dN = 6 \times 10^{-4}$ mm/cycle and $f = 20$ Hz. The macroscopic FCP direction is from bottom to top.

Stereofractographs showed that the striation profile on opposite sides of the crack plane resulted in mirror images, with the opposite fracture surfaces being closer to each other at the striations than in the regions between striations. Many small whitish points are present at the striations, with these points corresponding to the top of the fractured ligaments (Figs 9 and 12). The contrast enhancement effect obtained in scanning electron microscopy at peaks and sharp prominent corners make these regions appear white. These features indicate that the fatigue crack tip stretches or blunts between the striations, with actual fracture of ligaments occurring in the region of the striations.

The regions between as well as the regions of striations presented small U-shaped dimples (Fig. 12), similar to those in the large dimples, with the center of the U-edge all pointing in the direction from which the crack was originating. The features of these striations formed at high ΔK therefore indicate that their mechanism of formation involves blunting of the crack tip and coalescence with small microvoids ahead of this crack tip. For these striations, the microscopic crack growth direction coincided with the macroscopic crack growth direction in all regions. These observations thus show that the mechanism which forms the large dimples is related to that which forms the striations. The difference is that the large microvoids

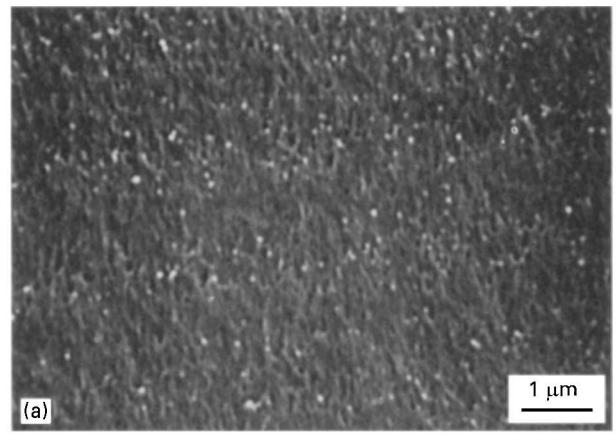

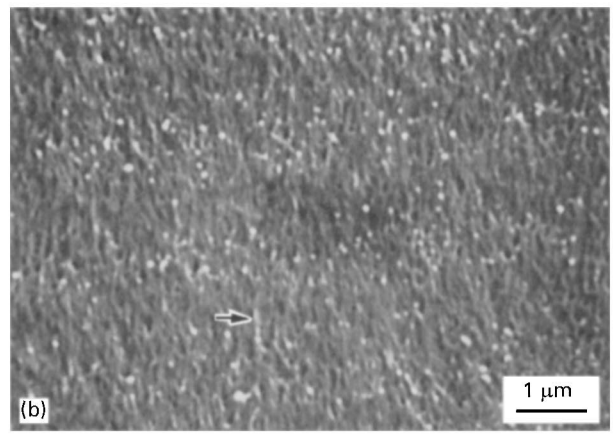

Figure 12 A pair of stereofractographs of striation-like features approximately 2 μm in width in a PS specimen for $\Delta K \approx 1.2$ MPa m$^{1/2}$, $da/dN \approx 2 \times 10^{-3}$ mm/cycle and $f = 2$ Hz. The macroscopic FCP direction is from bottom to top. A U-shaped dimple is pointed to by the arrow.

initiate by the formation of small microvoids approximately 0.1–0.4 μm ahead of the previous crack tip and then propagate in all directions (Fig. 8), while the region between striations is formed by crack growth occurring from the tip of the previous crack front and proceeding in the macroscopic crack propagation direction by a combination of crack tip stretching and of coalescence with small microvoids formed ahead of the previous crack tip (Fig. 12). The crack then arrests as the applied stress is decreased, with probably some crack tip resharpening occurring during this decreasing stress portion of the cycle. As the applied stress reincreases and becomes sufficiently large, crack growth restarts first by the fracture of ligaments in the vicinity of the arrested crack tip followed once more by crack tip stretching.

The interstriation spacing was measured on stereofractographs of the fatigue fracture surface of the PS specimens. Fig. 13 presents the interstriation spacing measured against the corresponding macroscopic FCGR. While most points showed reasonably good agreement between the crack growth rate and the interstriation spacing, some of the interstriation spacings measured were approximately two to three times the average da/dN measured at the same ΔK. Some of the observations even showed a strong local variation (approximately up to a factor of 5) in the interstriation spacing measured on fractographs corresponding to a region tested at essentially a constant nominal ΔK. One of the fractographic features observed on the full thickness specimens was that there was an approximately 0.6 mm thick surface layer in which the crack did not propagate at the same rate as in the remainder of the specimens, resulting in three fracture zones, one along each lateral surface and the other in the mid-thickness. This effect is caused by the well-known orientation effect in the skin region of injection-moulded specimens. The relationship between the striation spacing and da/dN was therefore verified at 20 Hz employing a modified CT specimen. Good agreement was then obtained between the interstriation spacing and da/dN (as also shown in Fig. 13) for all regions in which striations had formed. These results are consistent with the agreement between macroscopic and microscopic crack growth rates reported [25, 36] for various polymers including PS. These results strongly suggest that the poorer agreement obtained on the full-thickness specimens was associated with the presence of the surface layer causing the propagation near the mid-thickness region to be somewhat irregular at least for relatively high propagation rates. The results obtained thus indicate that the propagation per cycle at relatively high da/dN was equal to the interstriation distance, confirming that the striation-like features observed at high FCGRs in PS are indeed fatigue striations. Surface layers in which the propagation rate does not agree well with that in the mid-thickness can often occur when skin/core effects are observed which depend on the moulding process. Further work is needed to conclude on the effect of orientation on the FCP behaviour of the material tested.

The occasional presence of another type of band-like markings was also observed on the FCP fracture surface of the PS specimens. Fig. 14 shows approximately 120 μm large bands within which fatigue striations of approximate 10 μm spacing are present. This other type of marking appears similar to those in PMMA which have been referred to as ultrasonic fractographic markings [67]. Macroscopic ridge lines, separating regions of the fracture surface situated on slightly different but almost parallel planes, are also observed in Fig. 14.

The first crazes present in the final fracture region after the region of fatigue propagation of the PS specimens presented features (Fig. 15) which have been referred to as the "island" or "patch" pattern [68–70]. The depth of the individual fracture surfaces varies between two surfaces which are considerably further apart during the first portion of this pattern than during the second portion. The observations suggest

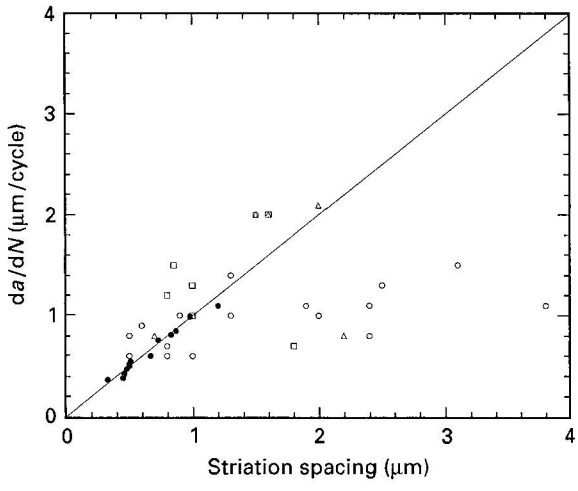

Figure 13 Comparison of the macroscopic FCGR (da/dN) and the striation spacing measured in PS specimens at 0.2 (△), 2 (□) and 20 Hz (○, ●). Closed symbols represent measurements on the modified CT specimen. A FCGR equal to the striation spacing (1 cycle = 1 striation) is indicated by the drawn line.

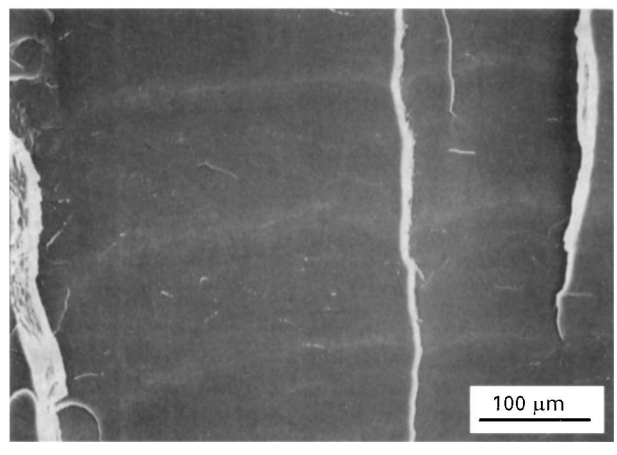

Figure 14 Low magnification micrograph in the striation region showing a regularly spaced (≈ 120 μm) wave-like variation of the crack plane in a PS specimen cycled at 20 Hz at high da/dN ($> 1 \times 10^{-3}$ mm/cycle). The macroscopic FCP direction is from bottom to top.

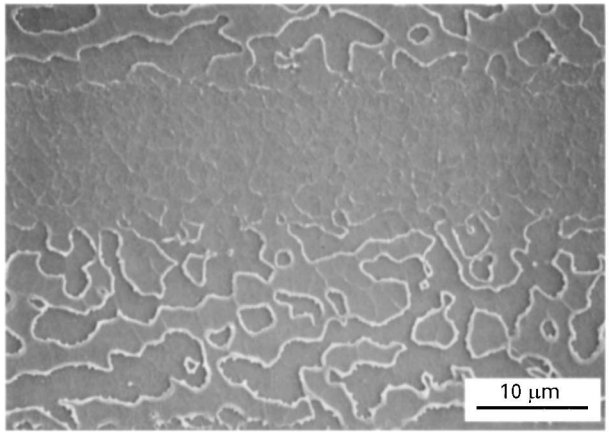

Figure 15 One of the first crazes (≈ 33 μm long) formed in the final fracture region of a PS specimen. The macroscopic FCP direction is from bottom to top.

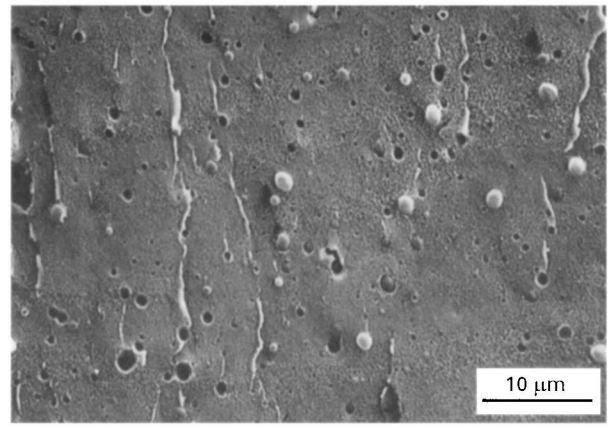

Figure 16 Micrograph showing the start of DGBs 6–8 μm in width observed in a non-compatibilized 95/5 PS/HDPE specimen for $\Delta K = 0.3$ MPa m$^{1/2}$, $da/dN = 2 \times 10^{-5}$ mm/cycle and $f = 20$ Hz. The macroscopic FCP direction is from bottom to top.

that at least the first portion of this pattern is produced by the crack advancing along patches situated along alternating craze–matrix interfaces. As indicated in Fig. 15, the difference in height between the craze patches decreases abruptly in the middle portion of these fractured crazes indicating that either the crazes get considerably thinner in this region or that the initial fracture planes change from situated at or near the two craze interfaces and become situated closer to the highly strained craze midrib [71, 72]. The presence of these two zones is in qualitative agreement with longitudinal strain measurements on fibrils along the craze width during DGB formation in PVC [39], showing that the fibril deformation is constant over approximately 50% of the craze width and then decreases closer to the craze tip, including results for PS [73, 74]. The difference in height observed between the craze patches, however, suggests that it is more probable that in the second zone the craze fractures near the midrib. Evidence for fibril elongation along the walls of the craze patches in this first portion in which there is a noticeable difference in depth between fast fracture regions is often noted. The fractographic features of the island pattern appears consistent with the increasing growth of microvoids observed with increasing f in the DGBs in the FCP region, since the increase in f increases ΔK for a given da/dN value.

3.5.2. Non-compatibilized 95/5 PS/HDPE specimens

The fatigue fracture surfaces of the 95/5 PS/HDPE specimens presented round dimples around HDPE particles (Figs 16 and 17), varying in size from approximately 0.1–1.5 μm, with the particle which had caused the appearance of each such microvoid usually present on one of the matching surfaces. The HDPE particles observed were approximately the size of the microvoids on the fracture surfaces at low ΔK, with the difference in size between the microvoids and the particles increasing with increasing ΔK but with this difference never becoming large. For crack growth rates up to approximately 1.6×10^{-4} mm/cycle, the

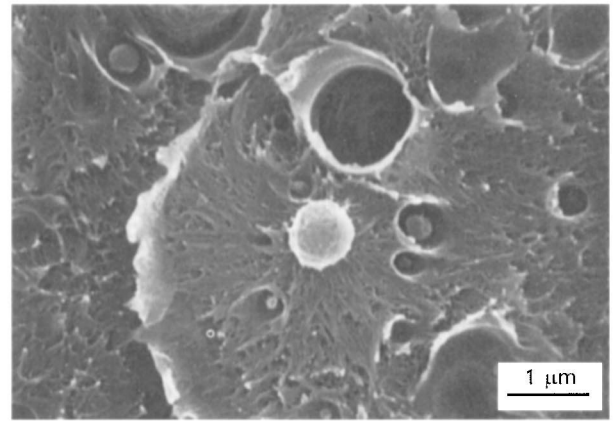

Figure 17 Micrograph at high magnification showing a large dimple-like feature formed around an HDPE particle in a non-compatibilized 95/5 PS/HDPE specimen for $\Delta K = 0.65$ MPa m$^{1/2}$, $da/dN = 9 \times 10^{-4}$ mm/cycle and $f = 0.2$ Hz. Fine U-shaped dimples pointing towards the HDPE particle located in the centre of the micrograph at which this large microvoid initiated can be observed. The macroscopic FCP direction is from left to right.

fracture surface presented DGBs which could be recognized by the presence of microvoids near their start, many of which had not formed at HDPE particles (Fig. 16). Many of these particles present near the start of a DGB were noticeably elongated, although this elongation was not very large, while HDPE particles present in the middle of DGBs were usually not noticeably elongated (Figs 16 and 18). Therefore the presence of the elongated HDPE particles could help situate the start of the DGBs when this was difficult to do from the small microvoids (not associated with HDPE particles) on the fracture surfaces. For $da/dN \approx 1 \times 10^{-4}$ mm/cycle, microvoids of approximately similar size were present throughout the DGB (Fig. 18). As well, HDPE particles, many of which give rise to ridge lines parallel to the FCP direction, can be noted in Figs 16 and 18, with the ridge lines initiating behind the particles. The breaks in these ridge lines are generally aligned, which helps identify the start of the DGBs, and suggests a discontinuous crack growth process.

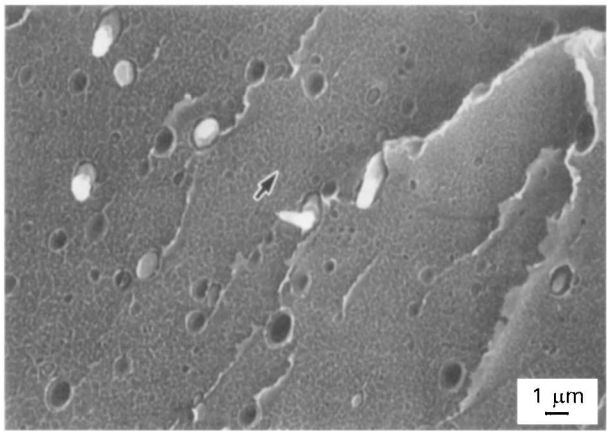

Figure 18 Micrograph showing the extremities of DGBs approximately 7 μm in width indicated by the presence of elongated HDPE particles and by ridge lines which have initiated behind these particles observed in a non-compatibilized 95/5 PS/HDPE specimen for $\Delta K = 0.3\ \mathrm{MPa\,m^{1/2}}$, $\mathrm{d}a/\mathrm{d}N = 1.3 \times 10^{-4}$ mm/cycle and $f = 0.2$ Hz. The FCP direction is indicated by the arrow.

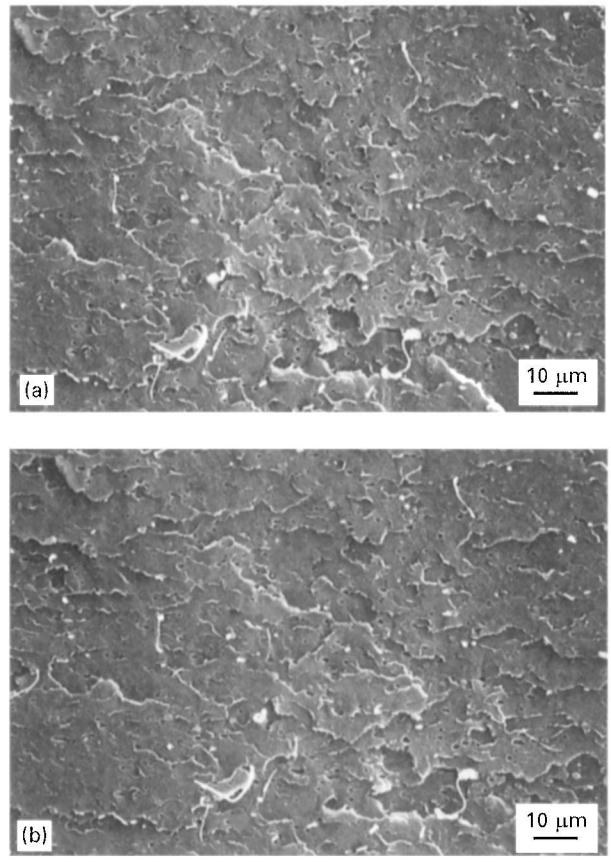

Figure 19 Stereofractographs of less clear DGBs approximately 10 μm in width which are indicated by changes in fracture surface height and by very elongated HDPE particles in a compatibilized 95/5 PS/HDPE specimen for $\Delta K = 0.65\ \mathrm{MPa\,m^{1/2}}$, $\mathrm{d}a/\mathrm{d}N = 1.2 \times 10^{-4}$ mm/cycle and $f = 20$ Hz. The macroscopic FCP direction is from left to right.

For crack growth rates slightly greater than 1.6×10^{-4} mm/cycle, large dimples (Fig. 17) approximately 0.5–3 μm in diameter were present, most of which had initiated as a microvoid around an HDPE particle, with the particle present on one of the matching fracture surfaces. Small U-shaped dimples indicating microvoids which had been incorporated into the large dimple often had not initiated at HDPE particles and had the centre of the U-edge pointing towards the initiation region of the large microvoid.

For $\mathrm{d}a/\mathrm{d}N$ greater than approximately $3–4 \times 10^{-4}$ mm/cycle, these large dimples became less continuous. Although more difficult to recognize than in the PS specimens, striation-like features generally could be detected well at higher FCGRs from the crests of the wave-like features on the FCP fracture surface using stereographic observations. Typical striation-like features are shown in Fig. 19. Such striations generally started near HDPE particles which were somewhat elongated. The sites of striations could often also be detected by the presence of discontinuous ridge lines which initiated behind HDPE particles (Figs 16 and 18), with these ridge lines often either not extending past the next striation or moving along this next striation.

The measurements of the interstriation spacing indicated that it was always considerably larger than the average amount of crack growth per cycle but was similar to the DGB spacing, with both the interstriation spacing and the DGB spacing increasing somewhat with increasing ΔK (Fig. 7b). The lack of agreement between the interstriation spacing and $\mathrm{d}a/\mathrm{d}N$ indicates that a number of cycles are required to form such a striation. Since the observations indicate that the HDPE particles near the start of a striation are somewhat elongated, this suggests that the presence of these particles retards the crack advance per cycle in the PS matrix until the decohesion of these HDPE particles occurs. The observations suggest that it is the particles near the striations which are particularly efficient in retarding the crack growth, which in turn suggests that it may be this crack blunting at each striation which causes some of these HDPE particles to act as more efficient obstacles to fatigue propagation.

As in the case of PS specimens, no effect of the cycling frequency on the DGB spacing in 95/5 PS/HDPE specimens was noted, but the DGBs showed an increasing microvoid size and a decreasing number of thin fibrils in the matrix with increasing f, similar to the effect of f on the DGB morphology in PS specimens (Fig. 6). Moreover, the number of microvoids per unit area which had formed at HDPE particles and which were observed on the fracture surface increased with decreasing f (Fig. 20) for all FCGRs. With increasing ΔK or FCGR, an increase in the number of HDPE particles and, consequently, also in the number of associated ridge lines was noted (Fig. 21).

3.5.3. Compatibilized 95/5 PS/HDPE specimens

The fracture surfaces of the compatibilized specimens (Figs 19 and 22) were quite similar to those observed for the non-compatibilized specimens in that many of the HDPE particles near the start of DGBs and near striations are elongated, with few of the particles in the middle of DGBs or between striations being

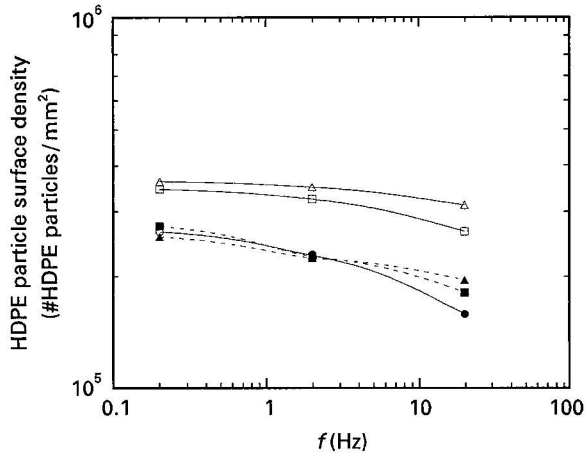

Figure 20 HDPE surface density plotted against f on a log–log scale in compatibilized and non-compatibilized 95/5 PS/HDPE for $\Delta K = 0.3$ (○, ●), 0.65 (□, ■) and 1.0 MPa m$^{1/2}$ (△, ▲). Open symbols represent non-compatibilized 95/5 PS/HDPE specimens. Lines are traced for compatibilized (– – –) and non-compatibilized specimens (——). For $\Delta K = 0.3$ MPa m$^{1/2}$, the three experimental points for the compatibilized specimens coincide almost exactly with those of the non-compatibilized specimens.

elongated. The amount of strongly elongated particles observed for the compatibilized blend, however, was much greater than for the non-compatibilized blend. This considerably greater elongation of particles in the presence of the compatibilizer suggests that its presence considerably increases the particle–matrix interfacial strength for many of the HDPE particles. Stereofractographic observations of the compatibilized blend specimens also revealed the presence of striation-like features, with an interstriation spacing considerably larger than the average da/dN value. Fig. 7b shows a variation of the DGB width and of the interstriation spacing as a function of ΔK in the 95/5 PS/HDPE specimens. As for the non-compatibilized blend, the spacings are similar to the DGBs and vary in approximately the same manner with ΔK as the DGBs. This suggests that in the two blends the DGBs and striation-like features are basically identical, although in the DGBs fine dimples not associated with HDPE particles are present, while these fine dimples are largely absent on the striation-like features formed above the intermediate values of da/dN at which large dimple-like features 1–3 μm in diameter form.

The da/dN value associated with the transition from DGBs to groups of dimples were measured as 1.7×10^{-4} mm/cycle at 2 Hz and 1.5×10^{-4} mm/cycle at 20 Hz in the 95/5 compatibilized blend, 1.6×10^{-4} mm/cycle for both frequencies in the non-compatibilized blend and $1.5–1.8 \times 10^{-4}$ mm/cycle at both frequencies for the PS specimens. Thus, the intermediate da/dN value at which large dimple-like features replace the DGBs is similar for all three materials.

The number of HDPE particles on the FCP fracture surfaces of the compatibilized and non-compatibilized blends was measured and is presented in Fig. 20 as the HDPE particle surface density plotted on a log–log scale against f. The HDPE particle surface density

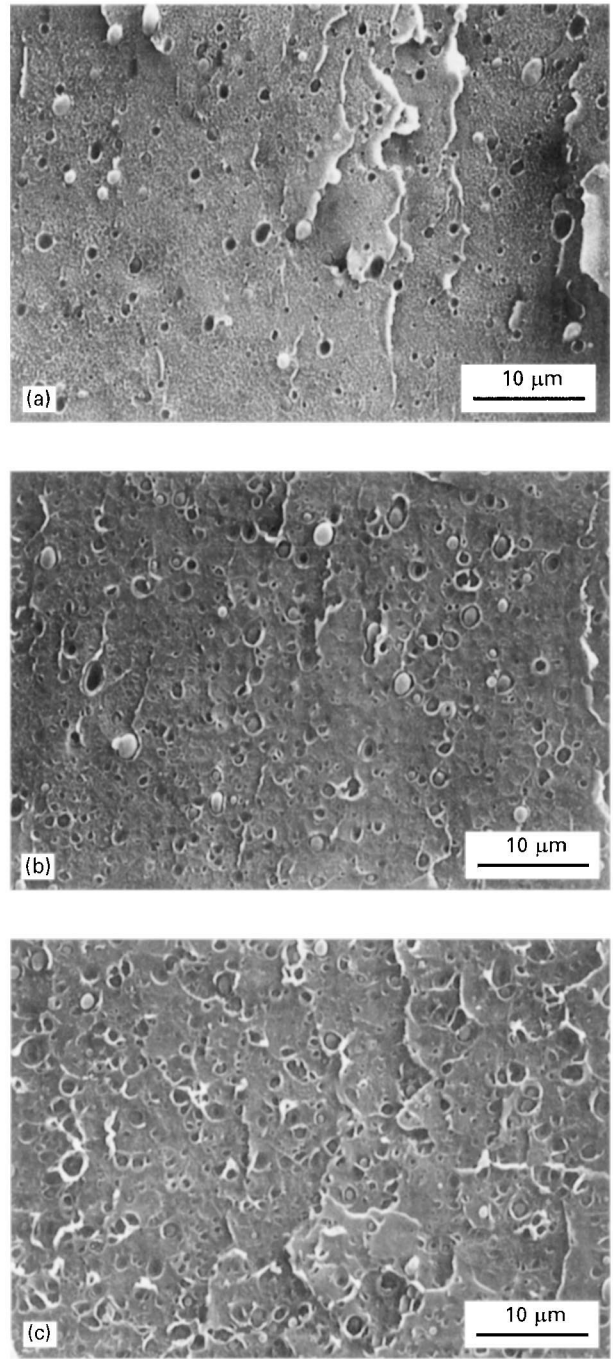

Figure 21 DGBs observed in a non-compatibilized 95/5 PS/HDPE specimen cycled at 2 Hz for: (a) $\Delta K = 0.3$ MPa m$^{1/2}$ and da/dN = 5×10^{-5} mm/cycle; (b) $\Delta K = 0.65$ MPa m$^{1/2}$ and da/dN = 3.6×10^{-4} mm/cycle, and (c) $\Delta K = 1.0$ MPa m$^{1/2}$ and da/dN = 1.1×10^{-3} mm/cycle. The macroscopic FCP direction is from bottom to top.

decreases with increasing f for both blends at all testing conditions. The HDPE particle surface density on the FCP fracture surface of the non-compatibilized specimens is considerably higher than that of the compatibilized specimens for all test frequencies for $\Delta K = 0.65$ and 1.0 MPa m$^{1/2}$. For $\Delta K = 0.3$ MPa m$^{1/2}$, the HDPE particle surface density is similar for both blends, indicating that at low ΔK the HDPE particle surface density on the fracture surface is not significantly affected by the presence of SEBS. The HDPE particle surface density increases with increasing ΔK in the absence of SEBS but varies

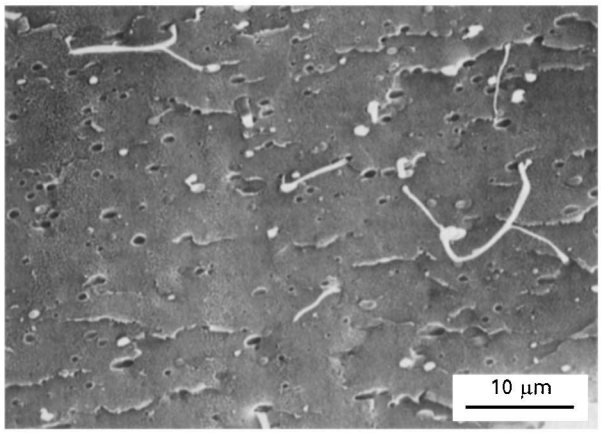

Figure 22 DGBs 5–6 μm in width showing a number of very elongated HDPE particles as well as associated ridge lines starting at such particles or at microvoids near the start of the DGBs in a compatibilized 95/5 PS/HDPE specimen for $\Delta K = 0.3$ MPa $m^{1/2}$, $da/dN = 2 \times 10^{-5}$ mm/cycle and $f = 20$ Hz. The macroscopic FCP direction is from left to right.

considerably less strongly with ΔK, in the presence of SEBS.

3.6. DGB formation

Stereofractographic observations of DGBs, especially in PS (e.g. Fig. 6), indicate that these DGBs were usually composed of three zones. A first zone of quite large dimples is formed along a thin line parallel to the crack tip and situated at the start of each DGB. The second zone is composed of relatively long fibrils with the interfibrillar spacing approximately constant at a given f. A third zone is composed of shorter fibrils, with a few quite large dimples near the end of this zone. These quite large dimples are similar to those in the first zone and are probably produced during the formation of the next DGB. Matching fracture surfaces showed that the third zone appeared as a depression on the matching fracture surfaces.

These observations indicate that in the second zone microvoids are formed at relatively large distances from each other in the direction perpendicular to the average fracture plane and probably at sites at or close to the two interfaces of the craze. In the third zone, the microvoids are formed at smaller distances from each other, resulting in shorter fibrils between the small microvoids. This difference in the length of the fibrils joining the microvoids in the second and third zones results in the fracture surface observed on stereofractographs being further from the outer extremity of the fracture plane in the third zone than in the two previous zones. Therefore if the microvoids in the third zone form at the two interfaces of the craze, the craze has to be considerably thinner in this zone, which suggests that it is more probable that the microvoids in this zone form near the midrib of the craze, in agreement with Döll *et al.* [39, 40]. The second and third zone of these DGBs therefore show strong similarities with the two zones of the fractured crazes produced at the start of the region of final fracture (Fig. 15), although the microvoids formed on the DGBs produced in fatigue are considerably smaller, especially for a low f.

These fractographic observations of DGBs therefore indicate that the detailed crack growth mechanism in a craze in the testing conditions employed here differs in detail from that proposed by Hull [75], in which the fracture occurs first near the craze midrib and then alternates between the interfaces of this craze. Fatigue fracture in DGBs by microvoid coalescence, however, has previously been proposed by Hertzberg and Manson [20].

3.7. Effect of cycling frequency

FCP tests on PS and the 95/5 PS/HDPE blends (Fig. 4 and Table II) showed a positive loading frequency effect in that increasing f reduced the crack propagation rate at a given ΔK, as previously observed on PS and on other thermoplastic polymers by Hertzberg *et al.* [20, 34]. However, the RMS spectrum (Fig. 2) only showed a weak such transition for the FCP conditions employed. In addition, the crack tip temperature rise measurements at the highest f employed only showed a maximum 0.5 °C temperature rise in the crack tip region. Such a temperature rise should be too weak to produce significantly enhanced yielding in the plastic zone during fatigue cycling, indicating that it is improbable that the positive frequency effect obtained is the result of the temperature rise in the crack tip region. Moreover, the tensile tests performed at different strain rates (Fig. 3 and Table I) showed that the strain rate did not strongly affect the tensile behaviour of the polymer tested, also indicating that the effect of f on the FCGR cannot be attributed to the strain rate strongly modifying the yield stress or Young's modulus. If a significant temperature rise existed in the plastic zone, the DGB spacing (Figs 6 and 7) as well as the HDPE particle surface density (Fig. 20) on the FCP fracture surface would be expected to increase with increasing f as a result of the larger plastic zone size caused by the enhanced yielding at the higher f associated with this local rise in temperature. In contrast, the DGB spacing measured is little affected by f, and the HDPE particle surface density decreases with increasing f. Therefore, the reduction of FCGR with increasing f in the present materials must be attributed to the nature of the fatigue crack growth and not to a change in temperature near the crack tip.

Observations of the DGBs on the FCP fracture surfaces of the different specimens provide important information on the deformation process leading to fracture. With increasing f, the size of the dimples observed in the second zone of the DGBs increases (Fig. 5). Because the DGB formation is attributed to the nucleation, growth and coalescence of dimples in the craze, these observations indicate that nucleation of microvoids is favoured at lower f while more growth of individual microvoids occurs at higher f; the higher number of cycles at higher f associated with the formation of a DGB at a given da/dN value contributes to producing this greater growth. The

plastic deformation in each cycle in the region of the crack tip is greater at lower f and the evidence indicates that this contributes to initiating more microvoids within the DGB present in the crack tip region. Therefore, the time available during each fatigue cycle for the craze to deform non-elastically should be an important parameter in the DGB formation. With more microvoids produced at lower f, the ligaments in the craze are thinner and should fracture by necking after fewer cycles. The same argument of the greater crack tip plastic deformation per cycle at a lower f should also account for the greater number of HDPE particles observed on the fracture surface at a lower f.

The average HDPE particle diameter has been evaluated by image analysis of cryomicrotomed specimens as 0.52 μm in the non-compatibilized blend and 0.45 μm in the compatibilized blend [10]. These particle diameters are considerably smaller than the widths of the DGBs (Fig. 7b); thus, the plastic strain zone in front of the crack tip contains a number of HDPE particles. However, the number of the HDPE particles per unit area of fracture surface decreases significantly with increasing f. Thus, craze nucleation at HDPE particles decreases in importance with increasing f, but the crack growth from each nucleation site increases with increasing f or with decreasing load application time per cycle. These observations suggest that a time-dependent effect similar to a creep effect must be considered for the FCP process. Such an effect has previously been proposed [25, 26, 30], but fractographic evidence supporting such an effect does not appear to have been presented previously.

3.8. Effect of HDPE addition with and without SEBS

In the blends, the widths of the DGBs observed at ΔK below the formation of large dimples and of the spacing between striation-like features observed at high ΔK followed a power-law relationship with ΔK^i (Fig. 7b), with the exponent i being 0.3 and 0.6 in the non-compatibilized and compatibilized blends, respectively. This indicates that the striation-like features observed at high da/dN in the blends very probably correspond to DGBs. While the fracture surfaces at high da/dN present few small dimples (not associated with HDPE particles), the number of such dimples on the DGBs observed at low da/dN decreases with increasing da/dN, which is in keeping with the striation-like features observed at high da/dN corresponding to DGBs essentially similar to those observed at low da/dN. The term DGB will therefore be henceforth employed to indicate the crack arrest markings observed at both high and low ΔK in these blends.

Although the tensile behaviour of PS was only slightly affected by the presence of 5% HDPE with and without SEBS (Table I), the FCP results (Fig. 4 and Table II) obtained showed that 5% HDPE led to a significant reduction in FCGR at cycling frequencies of 2 and 20 Hz, with this reduction being more important in the presence of the compatibilizer. At 0.2 Hz, however, the FCP results were similar for all three materials. In the blends, the number of HDPE particles on the fracture surfaces increased with increasing ΔK, suggesting that such particles acted as local crack initiation sites in front of the macroscopic crack tip, although this increase was much less important in the compatibilized blend.

In both blends, the large majority of HDPE particles which were noticeably elongated were those situated near DGB markings, with the particles between such markings usually not noticeably elongated. After the fatigue crack stops at such a marking, the local strain is greatest in the region of the crack tip. The HDPE particles in this region are therefore strained, assuming that they have sufficient cohesion with the matrix. The fracture at HDPE particles in the craze region ahead of the crack tip generally occurs by decohesion of not noticeably stretched particles at their interface with the PS matrix. The fracture at HDPE particles at the start of a DGB also generally occurs by such decohesion; however, these particles have often been noticeably stretched (Fig. 18) in the non-compatibilized blend and very strongly stretched (Figs 19 and 22) in the compatibilized blend, with fracture of some of the stretched particles in the compatibilized blend also appearing probable. The elongation of these particles indicates that their decohesion and fracture occurs behind the local crack front, and further behind this local crack front in the compatibilized blend than in the non-compatibilized blend. In both cases, the decohesion and fracture of the stretched particles behind the crack front seems to be associated with a bridging effect [76, 77].

These observations therefore suggest that the HDPE particles somewhat ahead of the start of a DGB initiate local cracks in the matrix around themselves, with these cracks producing decohesion at these particles, while the particles near the start of a DGB are stretched by the local strain. At least part of the increased resistance to fatigue crack propagation in the two blends is associated with the resistance to the decohesion or fracture of the HDPE particles present near the start of the DGBs, with this occurring very probably after the fracture of at least much of this DGB ahead of this crack tip. The decohesion at HDPE particles ahead of the start of each DGB may actually cause the initiation of cracks within a DGB to actually occur more rapidly than in the PS specimens at the same ΔK value.

In the presence of the SEBS compatibilizer, 5% HDPE improves more strongly the FCP resistance at 2 and 20 Hz. The fractographic observations then indicated that the elongated HDPE particles on the FCP fracture surface were much more elongated and that the number of HDPE particles on this surface increased considerably less rapidly with increasing ΔK for all test frequencies. These observations confirm that an efficient level of compatibilization was achieved. In this blend, the lower number of HDPE particles on the fracture surface suggests that the compatibilizer reduced the frequency of crack nucleation

at HDPE particles compared to the non-compatibilized blend. A possible explanation for this effect is that the presence of SEBS may have increased the stress required to initiate the fracture of crazes at particle–matrix interfaces.

At the lowest frequency employed (0.2 Hz), the blends had similar $\log da/dN$ versus $\log \Delta K$ curves as the PS polymer. At this frequency, the number of HDPE particles not noticeably stretched and not near the DGB interfaces was highest, and the decohesion of these particles can be expected to facilitate FCP. The plastic strain per cycle of the stretched HDPE particles near the start of the DGBs was presumably also more important at this low cycling frequency and the combined effect was not sufficient to result in improved resistance to fatigue crack propagation.

4. Conclusions

From the results of this study, it can be concluded that:

1. The addition of HDPE to PS, especially when SEBS is present with the HDPE, contributes to reducing the fatigue crack growth rates (FCGRs) at frequencies of 2 and 20 Hz but has little effect at 0.2 Hz.

2. Fractographic evidence of increased particle–matrix adhesion in the presence of SEBS is observed.

3. FCP occurs by the initiation, growth and coalescence of microvoids formed in the PS matrix and at HDPE particles when they are present.

4. In PS, DGBs are formed at low FCGRs with the DGB spacing varying with ΔK^i, the i exponent varying between 1 and 2. For FCGRs higher than $1.5–1.8 \times 10^{-4}$ mm/cycle, large dimple-like features are observed. For FCGRs higher than $3–4 \times 10^{-4}$ mm/cycle, fatigue striations are also observed with the large dimples becoming progressively less numerous with increasing FCGRs.

5. In PS/HDPE, DGBs are formed at all FCGRs except at intermediate FCGRs where large dimple-like features form. The DGB spacing varies approximately with ΔK^i, with the exponent i being 0.3 and 0.6 in the non-compatibilized and compatibilized PS/HDPE, respectively, indicating that the Dugdale or Irwin equations does not predict well the size of these DGBs. For FCGRs up to approximately 1.6×10^{-4} mm/cycle, the DGBs present microvoids near their start, many of which had not formed at HDPE particles. For FCGRs of approximately 1.6×10^{-4} mm/cycle to $3–4 \times 10^{-4}$ mm/cycle, the fracture surfaces present large dimples, most of which are initiated as a microvoid around an HDPE particle. For FCGRs greater than $3–4 \times 10^{-4}$ mm/cycle, these large dimples became less continuous and DGBs, which show elongated HDPE particles and corresponding discontinuous ridge lines near their start, are observed.

6. The FCGRs are reduced by a factor of 2–2.5 when the cycling frequency is increased by a factor of 10.

7. No significant temperature rise in the region of the plastically strained crack tip during FCP and no important strain rate effect on the tensile strength or Young's modulus of the materials tested were observed.

8. This effect of frequency is related to a time-dependent effect similar to a creep effect, with the plastic strain per cycle being significantly increased when the cycling frequency is decreased or the time per cycle is increased.

Acknowledgements

The authors are grateful to Dr Marc Prystay for assistance with the interpretation of results obtained with the infrared camera. Financial assistance from the NSERC (Canada) and FCAR (Québec) research support programmes is gratefully acknowledged.

References

1. B. BUCKNALL, in "Toughened plastics" (Applied Science Publishers, London, 1977) 359 pages.
2. W. M. BARENTSEN and D. HEIKENS, *Polymer* **14** (1973) 579.
3. D. HEIKENS and W. M. BARENTSEN, *ibid.* **18** (1977) 69.
4. C. R. LINDSEY, J. W. BARLOW and D. R. PAUL, *J. Appl. Polym. Sci.* **26** (1981) 1.
5. R. FAYT, R. JÉRÔME and PH. TEYSSIÉ, *J. Polym. Sci. Polym. Lett. Ed.* **19** (1981) 79.
6. T. APPLEBY, F. CSER, G. MOAD, E. RIZZARDO and C. STAVROPOULOS, *Polym. Bull.* **32** (1994) 479.
7. M. BOUSMINA, P. BATAILLE, S. SAPIEHA and H. P. SCHREIBER, *Comp. Interfaces* **2** (1994) 171.
8. H. EL KADI, J. DENAULT, D. TAPIN, M. F. CHAMPAGNE, L. A. UTRACKI and M. M. DUMOULIN, in Proceedings of the 53rd Annual Technical Conference, SPE, May 7–11 1994 (SPE, Boston, 1994) p. 3143.
9. M. N. BUREAU, H. EL KADI, J. DENAULT, J. I. DICKSON and S. FRÉCHINET, in Proceedings of the 54th Annual Technical Conference, SPE, May 5–9 1996 (SPE, Indianapolis, 1996) p. 2220.
10. M. N. BUREAU, H. EL KADI, J. DENAULT and J. I. DICKSON, *Polym. Eng. Sci.* **37** (1997) 377.
11. C. B. BUCKNALL, *Adv. Polym. Sci.* **27** (1978) 121.
12. A. S. ARGON, R. E. COHEN, O. S. GEBIZLIOGHI and G. E. SCHWIER, *ibid.* **52/53** (1983) 275.
13. S. WU, *Polymer* **26** (1985) 1855.
14. S. Y. HOBBS, *Polym. Eng. Sci.* **26** (1986) 74.
15. J. A. SAUER, J. TRENT and C. C. CHEN, *ibid.* **29** (1989) 69.
16. A. S. ARGON and R. E. COHEN, *Adv. Polym. Sci.* **91/92** (1990) 301.
17. G. DAGLI, A. S. ARGON and R. E. COHEN, *Polymer* **36** (1995) 2173.
18. J. P. ELINCK, J. C. BAUWENS and G. HONES, *Int. J. Fract. Mech.* **7** (1971) 277.
19. T. KUROBE and H. WAKASHIMA, *J. Soc. Mater. Sci.* **21** (1972) 800.
20. R. W. HERTZBERG and J. A. MANSON, *J. Mater. Sci.* **8** (1973) 1554.
21. R. W. HERTZBERG, J. A. MANSON and M. D. SKIBO, *Polym. Eng. Sci.* **15** (1975) 252.
22. R. W. HERTZBERG, in "Deformation and fracture mechanics of engineering materials" (John Wiley & Sons, New York, 1976) 605 pages.
23. R. W. HERTZBERG, J. A. MANSON and S. L. KIM, *J. Mater. Sci.* **12** (1977) 531.
24. A. S. ARGON and J. G. HANNOOSH, *Phil. Mag.* **36** (1977) 1195.
25. R. W. HERTZBERG, M. D. SKIBO and J. A. MANSON, ASTM STP **675** (1979) 471.
26. R. W. HERTZBERG and J. A. MANSON, in "Fatigue of engineering plastics" (Academic Press, New York, 1980) 295 pages.

27. C. B. BUCKNALL and P. DUMPLETON, *Polym. Eng. Sci.* **25** (1985) 313.
28. *Idem., ibid.* **27** (1987) 110.
29. M. T. TAKEMORI, *Adv. Polym. Sci.* **91/92** (1990) 263.
30. E. J. MOSKALA, *J. Appl. Polym. Sci.* **49** (1993) 53.
31. M. G. WYZGOSKI and G. E. NOVAK, *ibid.* **51** (1994) 873.
32. C. KOSTER, V. ALTSTÄDT, H. H. KAUSCH and W. J. CANTWELL, *Polym. Bull.* **34** (1995) 243.
33. E. J. MOSKALA, *J. Mater. Sci.* **31** (1996) 507.
34. M. D. SKIBO, R. W. HERTZBERG and J. A. MANSON, *ibid.* **11** (1976) 479.
35. N. J. MILLS and N. WALKER, *Polymer* **17** (1976) 335.
36. M. D. SKIBO, R. W. HERTZBERG, J. A. MANSON and S. L. KIM, *J. Mater. Sci.* **12** (1977) 531.
37. D. S. DUGDALE, *J. Mech. Phys. Solids* **8** (1960) 100.
38. G. PITMAN and I. M. WARD, *J. Mater. Sci.* **15** (1980) 635.
39. W. DÖLL and L. KÖNCZÖL, *Adv. Polym. Sci.* **91/92** (1990) 137.
40. M. G. SCHINKER, L. KÖNCZÖL and W. DÖLL, *Colloid Polym. Sci.* **262** (1984) 230.
41. M. KITAGAWA, *Bull. J. Soc. Mech. Eng.* **18** (1975) 240.
42. C. E. FELTNER, *J. Appl. Phys.* **38** (1967) 3576.
43. J. R. WHITE and J. W. TEH, *Polymer* **20** (1979) 764.
44. N. E. WATERS, *J. Mater. Sci.* **1** (1966) 354.
45. H. F. BORDUAS, N. H. WATTS and D. J. BURNS, *Polym. Eng. Sci.* **7** (1967) 90.
46. L. E. CULVER and D. J. BURNS, *J. Strain Anal.* **3** (1968) 193.
47. S. ARAD, J. C. RADON and L. E. CULVER, *J. Mech. Eng. Sci.* **13** (1971) 75.
48. B. MUKHERJEE and D. J. BURNS, *Exp. Mech.* **11** (1971) 433.
49. P. G. FAULKNER and J. R. ATKINSON, *J. Appl. Polym. Sci.* **15** (1971) 209.
50. J. C. RADON, *ibid.* **17** (1973) 3515.
51. R. W. HERTZBERG, J. A. MANSON and M. D. SKIBO, *Polymer* **19** (1978) 359.
52. R. ATTERMO and G. ÖSTBERG, *Int. J. Fract. Mech.* **7** (1971) 122.
53. D. HEIKENS, N. HOEN, W. M. BARENTSEN, P. PIET and H. LADAN, *J. Polym. Sci. Polym. Symp.* **62** (1978) 309.
54. R. FAYT, R. JÉRÔME and PH. TEYSSIÉ *J. Polym. Sci. Polym. Lett. Ed.* **19** (1981) 1269.
55. M. MATOS, P. LOMELLINI and B. D. FAVIS, in 52nd Proceedings of the Annual Technical Conference, SPE, May 1–5 1994 (SPE, San Francisco, 1994) p. 1517.
56. M. C. SCHWARZ, J. W. BARLOW and R. D. PAUL, *J. Appl. Polym. Sci.* **35** (1988) 2053.
57. R. FAYT, R. JÉRÔME and PH. TEYSSIÉ, *J. Polym. Sci. B, Polym. Phys.* **27** (1989) 775.
58. H. WELANDER and M. RIGDAHL, *Polymer* **30** (1989) 207.
59. S. B. RATNER and S. T. BUGLO, *Meck. Polim.* **5** (1969) 465.
60. J. D. FERRY, in "Viscoelastic properties of polymers", 3rd edition (John Wiley & Sons, New York, 1980) 641 pages.
61. K.-H. ILLERS, *Z. Electrochem.* **65** (1961) 679.
62. R. N. HAWARD, in "The physics of glassy polymers" (Halstead Press, New York, 1973) p. 41.
63. J. A. SAUER and C. C. CHEN, *Adv. Polym. Sci.* **52/53** (1983) 169.
64. P. C. PARIS and F. ERDOGAN, *J. Bas. Eng. Trans.: ASME Ser. D* **85** (1963) 528.
65. Y. M. MAI and J. G. WILLIAMS, *J. Mater. Sci.* **14** (1979) 1933.
66. J. S. HARRIS and I. M. WARD, *ibid.* **8** (1973) 1655.
67. K. TAKAHASHI and S. HYODO, *J. Macromol. Sci.-Phys.* **B19** (1981) 695.
68. D. HULL, *J. Mater. Sci.* **5** (1970) 357.
69. J. MURRAY and D. HULL, *Polymer* **10** (1969) 451.
70. *Idem., ibid. J. Polym. Sci. A2* **8** (1970) 583.
71. P. BEAHAN, M. BEVIS and D. HULL, *Polymer* **14** (1973) 96.
72. *Idem., ibid. Proc. R. Soc. London Ser. A* **343** (1975) 525.
73. B. D. LAUTERWASSER and E. J. KRAMER, *Phil. Mag.* **A39** (1979) 469.
74. E. J. KRAMER, *Adv. Polym. Sci.* **52/53** (1983) 1.
75. D. HULL, in "Polymeric materials" (ASM, Metals Park, OH, 1975) 487 pages.
76. H. R. AZIMI, R. A. PEARSON and R. W. HERTZBERG, *J. Mater. Sci. Lett.* **13** (1994) 1460.
77. H. R. AZIMI, R. A. PEARSON and R. W. HERTZBERG, *J. Mater. Sci.* **31** (1996) 3777.

Received 11 November 1996
and accepted 23 October 1997